

https://doi.org/10.1070/QEL16267

Postionisation of a spatially nonuniform plasma plume under high-intensity femtosecond laser irradiation*

D.A. Krestovskikh, K.A. Ivanov, I.N. Tsymbalov, S.A. Shulyapov, V.V. Bukin, R.V. Volkov, A.A. Rupasov, A.B. Savel'ev

Abstract. **The plasma plume formed by a high-power nanosecond laser pulse on the surface of solid targets as well as the plume parameters after its irradiation by a high-intensity femtosecond laser pulse are investigated by optical diagnostic techniques. Two-dimensional patterns of the electron plasma density are reconstructed from experimentally recorded interferograms at different stages of plasma evolution. It is shown that the interaction of the high-intensity femtosecond radiation with the plasma cloud is accompanied by the field ionisation of atoms and ions as well as by a significant increase in the electron density throughout the interaction volume.**

Keywords: *laser-produced plasma, high-power laser pulses, interferometry, electron density, ionisation.*

1. Introduction

The progress in laser technology has led to the development of systems capable of generating laser pulses of petawatt power and of duration down to several tens of field cycles, which permits attaining at-focus intensities above 10^{22} W cm^{-2} [1]. The interaction of such radiation with a substance (be it a gas, a liquid, or a solid) gives rise to a hot, nonequilibrium, and strongly ionised laser-produced plasma, whose electrons may gain energies up to tens of MeV [2–10]. This plasma also emits radiation in a broad wavelength range: from bremsstrahlung and line X- and gamma-rays to UV and visible radiation. On the whole, this plasma finds increasingly wide application in basic and applied research [11].

Numerical simulations of laser-plasma interactions, which are most often implemented with the use of PIC codes, are a significant component of research in the field of high-intensity laser radiation interaction with plasmas [10, 12, 13]. In this case, there is no way of reaching adequate agreement between simulations and experimental data when the numerical simulations make no use of the spatial distribution of the electron density corresponding to real experimental conditions. Specifically, discovered in the recent investigations performed in our group [14] was a significant increase in the energy of hot electrons when the plasma preproduced by a nanosecond pulse was irradiated by a femtosecond laser pulse for an intensity above 10^{18} W cm^{-2}. Numerical simulations performed in this case revealed the decisive role of the plasma profile in the course of electron acceleration.

The studies of the plasma plume produced by laser pulses of different duration are widely covered in the literature [15, 16]. In particular, actively employed for these purposes are optical probing techniques – shadowgraphy, interferometry, etc. The task of investigating the plasma expansion becomes more important when we are dealing with laser pulses of relativistic intensity. This is due to two circumstances. First, with increasing intensity of the main laser pulse, the prepulse intensities also become higher (characterised by the so-called contrast ratio of the laser pulse, i.e. by the relative prepulse amplitudes on the nano- and picosecond time scales). Even for a presently attainable contrast ratio of 10^{-10} and better [17], the prepulse intensity may turn out to be sufficiently high for producing an extended preplasma. Therefore, the existence of a preplasma is unavoidable, especially when dense metallic targets are under irradiation. Second, the intensity of the main laser pulse at the beam waist is sufficiently high for the field ionisation of preplasma atoms and ions. This is responsible for energy dissipation and, in special cases, to beam defocusing and a lowering of the intensity at the target [18].

In the present work we investigate the temporal dynamics of the plasma produced on the surface of solid targets by two, nanosecond and femtosecond, high-power laser pulses with the use of shadowgraphy and optical interferometry. The action of the high-power nanosecond Nd:YAG laser radiation models the contribution of one of the main prepulse components – the amplified spontaneous luminescence, which also is of nanosecond duration. It is shown that the propagation of a high-intensity femtosecond laser pulse through such preplasma leads to its significant ionisation.

2. Schematic of the experimental facility

To produce the plasma on the target surface, use was made of the pulsed Nd:YAG laser radiation with a wavelength of 1064 nm, a pulse duration of ~10 ns, a pulse energy of ~100 mJ, and a pulse repetition rate of 10 Hz (Fig. 1). An off-

* Presented at ECLIM2016 (Moscow, 18–23 September 2016).

D.A. Krestovskikh, I.N. Tsymbalov, S.A. Shulyapov, R.V. Volkov, A.B. Savel'ev Department of Physics and International Laser Centre, M.V. Lomonosov Moscow State University, Vorob'evy Gory, 119991 Moscow, Russia; e-mail: kda4991@gmail.com;
K.A. Ivanov Department of Physics and International Laser Centre, M.V. Lomonosov Moscow State University, Vorob'evy Gory, 119991 Moscow, Russia; P.N. Lebedev Physics Institute, Russian Academy of Sciences, Leninsky prosp. 53, 119991 Moscow, Russia;
V.V. Bukin A.M. Prokhorov General Physics Institute, Russian Academy of Sciences, ul. Vavilova 38, 119991 Moscow, Russia;
A.A. Rupasov P.N. Lebedev Physics Institute, Russian Academy of Sciences, Leninsky prosp. 53, 119991 Moscow, Russia

Received 5 December 2016
Kvantovaya Elektronika **47** (1) 42–47 (2017)
Translated by E.N. Ragozin

axis parabolic mirror with a focal length-to-diameter ratio $F/D = 5$ focused the radiation onto the target surface. The at-focus radiation intensity amounted to $\sim 10^{12}$ W cm^{-2}. Experiments were performed with molybdenum and plastic (PMMA) targets made in the form of thick flat plates. The radiation was incident at an angle of 45° to the normal to the target surface.

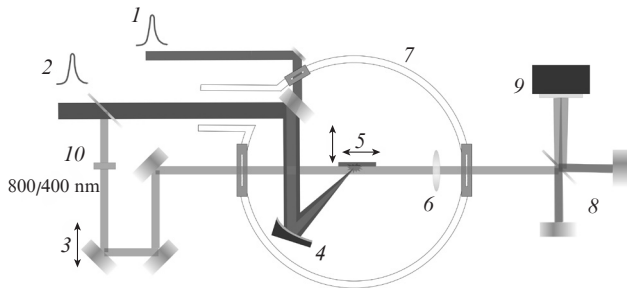

Figure 1. Experimental setup:
(*1*) Nd : YAG laser radiation; (*2*) Ti : sapphire laser radiation; (*3*) delay line; (*4*) parabolic mirror; (*5*) target; (*6*) imaging lens; (*7*) vacuum chamber; (*8*) Mickelson interferometer; (*9*) CCD matrix; (*10*) KDP crystal for second harmonic generation.

To irradiate and diagnose the preproduced plasma, we used the Ti : sapphire laser radiation with a wavelength of 800 nm, a pulse duration of ~50 fs, and a pulse repetition rate of 10 Hz. The delay between the plasma-producing pulse and the Ti : sapphire laser pulse was varied with an electric timing circuit from –10 ns (the femtosecond pulse arrives at the target prior to the nanosecond one) to +30 ns with a time jitter of 1 ns. Part of the femtosecond radiation was diverted with a beam splitter, passed via a precision delay line, and was directed along the target surface for constructing the optical plasma image.

Two series of experiments were carried out. In the first one (single-pulse irradiation) the plasma was produced only by a nanosecond pulse; in the second series, the plasma produced by a nanosecond pulse was next irradiated by a femtosecond pulse (two-pulse irradiation). In the latter case, part of the femtosecond radiation (with an energy of ~2 mJ) was focused onto the target by the same parabolic mirror as the nanosecond radiation. To this end, we used a mirror transparent at a wavelength of 1064 nm and reflective at 800 nm. The peak (in-vacuum) intensity of the heating femtosecond pulse amounted to $\sim 10^{17}$ W cm^{-2}. The spatial superposition of the femtosecond and nanosecond pulses on the target was monitored with a microlens, which imaged the transverse plane at the beam waist to a CCD camera. The superposition was accurate to within ~5 μm (the diameters of the beam waists were equal to about 20 μm for Nd : YAG laser pulses and to 2.5 μm for femtosecond pulses). The probing femtosecond pulse was delayed relative to the heating femtosecond pulse by about 1 ps with the use of a precision delay line. The temporal match was monitored from the interference of the two beams at the target and was accurate to about the pulse duration (50 fs).

The probing radiation transmitted through the plasma was transferred to a CCD matrix via a Michelson interferometer with the use of a 10-fold magnifying lens with a focal length of 6 cm. In several experiments involving two-pulse target irradiation, the probing radiation frequency was doubled in a KDP crystal to decrease the parasitic background noise arising from the radiation of the heating femtosecond pulse scattered by the plasma and the optical components.

Since the electron density of the plasma is related to its refractive index and the spatial distribution of the addition to the refractive index is related to the spatial distribution of the phase shift of the radiation transmitted through the plasma, by processing interferograms it was possible to obtain the spatial distribution of the electron plasma density. We also measured plasma shadowgrams when one of the Michelson interferometer arms was blocked.

3. Main results

Figure 2 depicts an interferogram obtained by probing the plasma produced on the molybdenum target surface (for a zero delay, i.e. when the peaks of the heating and probing pulses coincided) and the corresponding two-dimensional electron density distribution in the plasma region transparent for the optical radiation. One can see a dark near-target plasma region, in which the electron density N_e is higher than the critical density N_{cr} of the given probe radiation wavelength. However, it is pertinent to note that the boundary of the dark region corresponds to the plasma density approximately one order of magnitude lower than the critical density because of a strong dissipation and scattering of the probing radiation in its passage through the plasma layer.

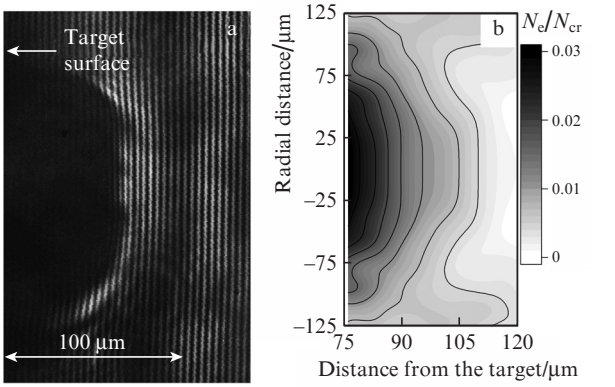

Figure 2. (a) Plasma interferogram for a zero time delay between the heating and probing pulses and (b) the corresponding axially symmetric electron density distribution.

Apart from the interferograms of the laser-produced plasma, we also recorded the interferograms of empty space. The phase shift distributions obtained for each pair of the interferograms were subtracted from each other. In this way it was possible to get rid of the constant inclined constituent and other distortions of the wavefront not related directly to the plasma. Assuming the plasma plume to be axially symmetric, we apply the inverse Abel transform [19] to the resultant spatial phase distribution to obtain the addition to the refractive index

$$\Delta n(x,r) = -\frac{\lambda}{2\pi^2}\int_r^\infty \frac{\varphi_y'(x,y)}{\sqrt{y^2-r^2}}\,\mathrm{d}y, \qquad (1)$$

where $\varphi'_y(x,y) = d\varphi(x,y)/dy$; x is the coordinate along the target normal; λ is the probing radiation wavelength; y is the coordinate along the target in the image plane; and $\varphi(x,y)$ is the phase at the corresponding point of the interferogram. Using the collisionless limit of the Drude model, which relates the plasma refractive index n to the electron density N_e, $n^2 = 1 - N_e/N_{cr}$ [20], we then obtain the spatial distribution of the electron plasma density. For a wavelength of 800 nm, $N_{cr} = 1.8 \times 10^{21}$ cm^{-3}. The processing was performed employing the IDEA software [21]; in this case, the measurement uncertainty was equal to $\sim 0.005 N_{cr}$.

In addition to the interference plasma images, shadow photographs of the plasma were also recorded for the primary analysis of the expansion dynamics of the hot cloud. Figure 3 shows the size of the opaque region of molybdenum and PMMA plasmas in relation to the delay between the probing and heating pulses, which was obtained from shadow plasma diagnostics.

With reference to Fig. 3, the opaque plasma boundary recedes from the target surface while there is the influx of energy from the heating pulse. The expansion velocity of the molybdenum plasma cloud at the heating stage may be estimated at $\sim 10^4$ m s^{-1}. For PMMA, however, this velocity is somewhat lower and amounts to 4×10^3 m s^{-1}. A simple estimate of the ion sound velocity $v_i = \sqrt{ZT_e/M_i}$ [22] (where Z is the ionisation rate; T_e is the plasma temperature; and M_i is the ion mass) yields a figure of $\sim 4 \times 10^3$ m s^{-1} for molybdenum and of 10^4 m s^{-1} for PMMA for $Z = 1$ and a plasma temperature of about 10 eV typical for our experimental conditions [23, 24]. We nevertheless believe that the experimentally obtained estimate does not correspond to the real plasma expansion velocity in this case. The matter is that, first, for a time delay of up to 5 ns the plasma is still heated by the laser pulse of the Nd:YAG laser. Second, the bulk of the pulse energy is absorbed in the near-critical density layer. Therefore, the ionisation occurs in the plasma layer permanently receding from the target rather than at the target surface. Furthermore, for molybdenum the longitudinal cloud dimension turns out to be longer due to the greater number of electrons resulting from ionisation (both due to the higher material density and to the lower ionisation energy in comparison with PMMA).

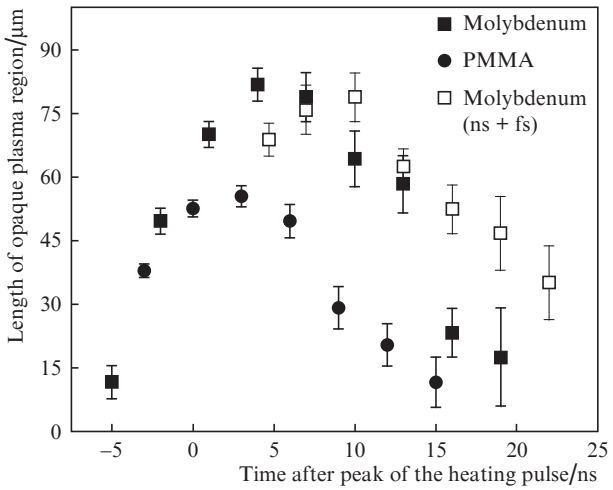

Figure 3. Length of the opaque plasma region along the normal to the target surface as a function of probing pulse delay for the PMMA target and the metallic (molybdenum) target, as well as for a two-pulse irradiation of the molybdenum target (see Section 4).

After cessation of the heating, the opacity front stops and in 12 ns after the passage of the peak of the heating pulse the plasma begins to cool down while continuing to expand in vacuum. Since the intensive ablation terminates, the total mass of the plume remains invariable while increasing in volume. This has the effect that the boundary of the part of the cloud which is opaque to the probe radiation begins to move back to the target surface.

To investigate the plasma dynamics in greater detail, we consider the electron density profiles on the central axis of the cloud at different moments of its evolution (Fig. 4). It is significant that the highest value of the electron density which is possible to obtain from the interferograms amounts to $\sim 10^{20}$ cm^{-3}. This is due to the strong refraction of the probing radiation in its passage through the near-critical plasma region of thickness ~ 100 μm, which is clear from the increase in image brightness near the boundary of the opaque region.

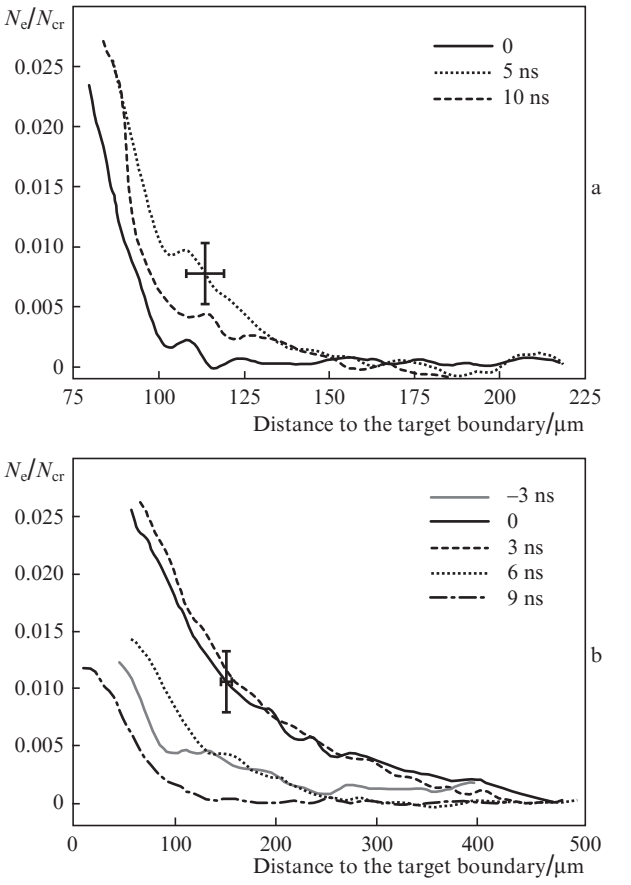

Figure 4. Electron density profiles on the central plasma axis for different time delays after the action of the heating nanosecond pulse for (a) molybdenum and (b) PMMA targets.

For the metal target (Fig. 4a) for delay times of 0–5 ns, when there is an energy influx from the nanosecond pulse, the electron density rapidly decreases from the highest detectable density to practically zero in a distance of about 50 μm. At the same time, the profile itself is rather complicated in shape, which, generally speaking, cannot be approximated with one

exponential function throughout the range of distances from the target plane. The rather sharp decrease may be attributed, as mentioned above, to the permanent motion of the critical layer in the opposite direction to the incident radiation.

As the time delay increases to 10–15 ns, the subcritical layer is at the longest distance from the target surface in agreement with the data of shadow diagnostics. The steepness of an electron density decrease becomes smaller with distance from the surface. After cessation of the radiation-induced heating, the critical layer begins to expand and plasma profile rapidly becomes gradual.

For a time delay of 20 ns and over, the plasma becomes so transparent to the radiation that it does not introduce phase shifts detectable in our experimental setup. Nevertheless it should be noted that the phase shift in the interferograms, which is determined by the presence of free electrons in the plasma, may be absent because of rather strong plasma recombination for long delays. That is, generally speaking, the electron density profile does not reproduce the ion (atom) density distribution for longer temporal delays.

It is significant that a direct extrapolation of the profile to the higher-density region (above $0.1N_{cr}$) would not be quite correct, because, as indicated above, the energy input takes place in the critical region, which cannot be diagnosed by optical interferometry. As shown in Ref. [25], even in the case of a one-dimensional expansion the plasma profile is complex throughout the distance from the target surface.

In contrast to the data of shadow diagnostics (i.e. the diagnostics the higher-density plasma region) the results for the PMMA target turned out to be better predictable in the region with a density well below the critical one. Even at the peak of the heating pulse, the subcritical region is much farther (up to 400 μm) from the target surface than for the metal target (up to 150 μm). This is consistent with the fact that the expansion velocity of the lighter target is higher. The more gradual profile of the plasma itself may be attributable to a lower ionisation of atoms in the plastic target case. Furthermore, because of the higher expansion velocity the PMMA plasma vanishes almost completely for times longer than 10 ns, as is evident from Fig. 4b and from the data of shadow diagnostics.

4. Additional plasma photoionisation under femtosecond pulse irradiation

When it comes to investigating the interaction of a high-power femtosecond pulse with an expanding plasma, an important role is played by the field ionisation of the plasma under the action of the front of the incident pulse. Modern theories quite often disregard this circumstance. It may nevertheless make a significant contribution to the properties of the expanding plasma.

As pointed out in Section 1, we investigated the effect of additional heating femtosecond radiation of high intensity on the plasma produced by a nanosecond pulse. These experiments were performed for the metal target. In this case, the time delay between the femtosecond and probing pulses was equal to about 1 ps.

Figure 3 shows the position of the front of opaque plasma region at different points in time after nanosecond pulse irradiation in the case of such two-pulse irradiation regime (molybdenum, ns + fs). The effect on the front position exerted by the second pulse is strongest after the termination of plasma heating by the longer pulse, i.e. when the plasma is 'left to itself' from the viewpoint of its expansion in vacuum. The increase in size of the opaque region (i.e. additional ionisation) is also seen at times longer than 15 ns, when the interferometric diagnostics turns out to be helpless. The latter is consistent with the assumption made above that the plasma recombines for long delay times.

The on-axis (for $r = 0$) profiles of the electron density with and without femtosecond pulse irradiation of the plasma are compared in Fig. 5. Since the probing pulse wavelength was equal to 400 and not 800 nm (to avoid the parasitic illumination by the radiation scattered by the plasma), the highest attainable density turned out to be higher (of the order of $0.04N_{cr}$). One can see a departure of the region of a steep density decrease from the target surface, which is related to the field ionisation by the femtosecond heating pulse. The effect is most pronounced for a time delay of about 10 ns. In this case, the electron density increases by about a factor of two along the whole length of the subcritical cloud.

It is significant that the electron density increases not only in the region of the laser beam waist, which measures less than 20 μm in length in our conditions. This is due to the fact that even at a distance of ~100 μm from the focal plane the radiation intensity amounts to 5×10^{13} W cm^{-2}, i.e. the probability of the field ionisation of the electrons with a binding energy of ~10 eV becomes high.

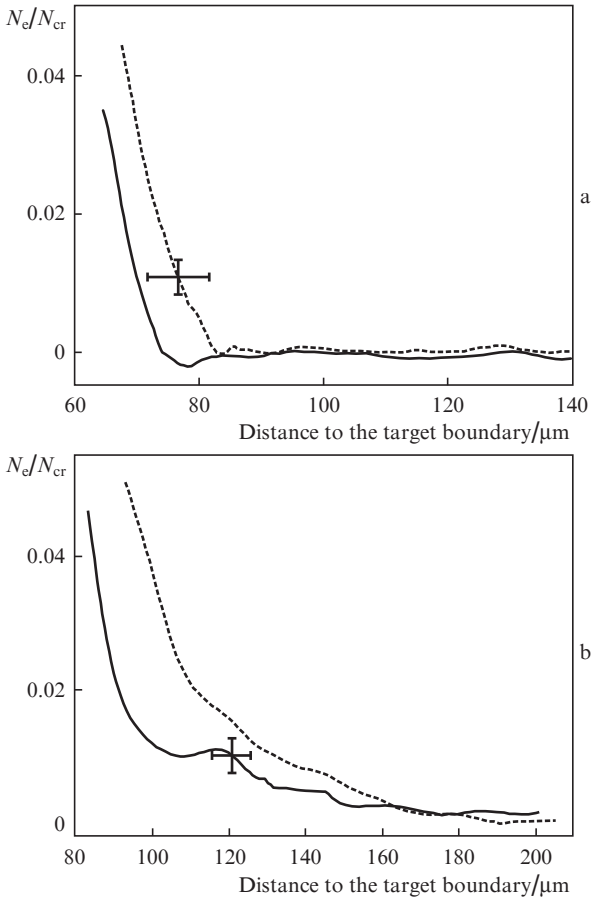

Figure 5. Electron density profiles along the central plasma axis in the case of additional femtosecond pulse irradiation (dashed curves) and without it (solid curves) at the points in time equal to (a) 0 and (b) 10 ns after the peak of the nanosecond pulse.

5. Numerical estimate of the field ionisation of the plasma by the femtosecond radiation of subrelativistic intensity

According to the Drude model, the electron density is related to the refractive index of the plasma, and therefore an increase in the electron density will affect the focusing of radiation passing through the plasma, which leads to a change in the region of radiation absorption in the plasma changes. This in turn may result in ionisation-induced defocusing [18], which hampers the attainment of the rated peak intensity of a femtosecond laser pulse. As is commonly known, the efficiency of one or other mechanism of fast-electron acceleration depends heavily, among other things, on the intensity [26, 27], whence we may draw a conclusion that the additional plasma ionisation affects to a considerable degree the gain of energy by particles.

To estimate the effect of ionisation on the parameters of radiation focusing we performed numerical calculations of the field ionisation of the plasma by a femtosecond pulse. For this purpose we used a 2D model for the propagation of a linearly polarised focused Gaussian beam through the plasma. The relation between the field intensity vector E of the femtosecond pulse and the plasma characteristics was defined with the wave equation and the Drude model. For plasma parameters we employed the values and profile of the electron density obtained from our experiment (Fig. 5b); however, the profile was smoothed out to avoid undesirable simulation errors. The femtosecond radiation intensity was set equal to the in-vacuum intensity of the femtosecond pulse in the experiment conducted, which amounts to $\sim 10^{17}$ W cm^{-2}. To calculate the field ionisation, we used the kinetic equation:

$$\frac{\mathrm{d}N_i}{\mathrm{d}t} = W_i N_{i-1} - W_{i+1} N_i, \tag{2}$$

where N_i is the density of atoms in the ith ionisation state; W_i is the ionisation probability defined by expression [28, 29]

$$W(E) = 4\omega_\mathrm{a} r_\mathrm{H}^{5/2} \frac{E_\mathrm{a}}{\langle E(t)\rangle} \exp\left(\frac{-2 r_\mathrm{H}^{3/2} E_\mathrm{a}}{3\langle E(t)\rangle}\right), \tag{3}$$

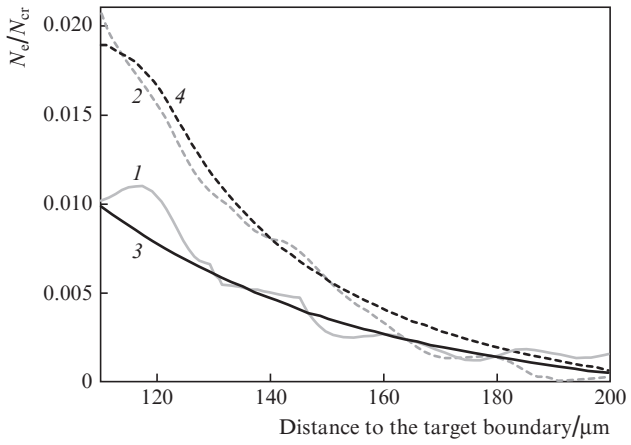

Figure 6. Comparison of the simulated and experimental profiles of the electron density: (*1*) experimental profile without a femtosecond heating pulse, a 10-ns delay, (*2*) experimental profile with the femtosecond heating pulse, (*3*) initial profile in the numerical model, (*4*) simulated profile after passage of the femtosecond pulse.

where ω_a and E_a are the atomic frequency and the atomic field; $r_\mathrm{H} = E_\mathrm{i}/E_\mathrm{H}$; and E_i and E_H are the ionisation potentials of the corresponding (molybdenum) ion and hydrogen. The electric field in expression (3) is averaged over one cycle of the electromagnetic wave. The electron density is calculated from the relationship

$$n_\mathrm{e} = \sum_i i N_i. \tag{4}$$

The numerical and experimental results for plasma ionisation are compared in Fig. 6. One can see that these data are similar, and the experimentally observed approximately twofold increase in the electron density of the plasma plume is indeed attributable to the field ionisation of the preplasma by the femtosecond laser pulse.

6. Conclusions

Therefore, we have studied the dynamics of the plasma cloud produced by high-power nanosecond radiation on the surface of solid targets and the ionisation of the plasma cloud by an additional femtosecond pulse. Optical diagnostics by shadow photography and interferometry showed that the plasma on the surface of a solid target has a complex spatial profile, which cannot be approximated with a single exponent. In this case, the motion of the boundary of opaque plasma region away from the target with a velocity of the order of the ion-sound velocity terminates immediately after the cessation of the laser pulse and, several nanoseconds later, this boundary begins moving towards the target. It was experimentally determined that the interaction of femtosecond radiation with this plasma results in a significant increase in its electron density due to field ionisation. This effect may be responsible for significant changes of the peak intensity of the femtosecond radiation due to ionisation-induced defocusing. A significant suppression of the effect of preplasma postionisation would be expected with the use of targets with a low atomic number.

It should be noted that the effect of preplasma postionisation discovered in our work may play an even more significant role as the intensity of laser radiation increases into the relativistic domain and that it should undoubtedly be included in the simulation of laser-plasma interactions in this intensity regime.

Acknowledgements. This work was supported by the Russian Foundation for Basic Research (Grant Nos 16-02-00263 and 16-02-00302). K.A.Ivanov acknowledges the support of the Russian Foundation for Basic Research (Grant No. 16-32-60174_mol-a-dk).

References

1. Mourou G., Tajima T., Bulanov S. *Rev. Mod. Phys.*, **78**, 309 (2006).
2. Giulietti D., Gizzi L.A. *Riv. Nuovo Cimento*, **21**, 1 (1998).
3. Umstadter D. *J. Phys. D: Appl. Phys.*, **36**, R151 (2003).
4. Kryukov P.G. *Kvantovaya Elektron.*, **31**, 95 (2001) [*Quantum Electron.*, **31**, 95 (2001)].
5. Sentoku Y., Cowan T.E., Kemp A., Ruhl H. *Phys. Plasmas*, **10**, 2009 (2003).
6. Shulyapov S.A., Mordvintsev I.M., Ivanov K.A., Volkov R.V., Zarubin P.I., Ambrozova I., Turek K., Savel'ev A.B. *Kvantovaya Elektron.*, **46**, 432 (2016) [*Quantum Electron.*, **46**, 432 (2016)].
7. Ivanov K.A., Uryupina D.S., Morshedian N., Volkov R.V., Savel'ev A.B. *Fiz. Plazmy*, **36**, 115 (2010).

8. Wilks S.C., Langdon A.B., Cowan T.E., Roth M., Hatchett S., Key M.H., Pennington D., MacKinnon A., Snavely R.A. *Phys. Plasmas*, **8**, 542 (2001).
9. Yang L., Deng Z.G., Yu M.Y., Wang X.G. *Phys. Plasmas*, **23**, 083106 (2016).
10. Huang Y., Wang N., Tang X., Shi Y., Xueqing Y. *Phys. Plasmas*, **19**, 093109 (2012).
11. Roth M., Cowan T.E., Key M.H., Hatchett S.P., Brown C., Fountain W., Johnson J., Pennington D.M., Snavely R.A., Wilks S.C., Yasuike K., Ruhl H., Pegorano F., Bulanov S.V., Campbell E.M., Perry D.M., Powell H. *Phys. Rev. Lett.*, **86**, 436 (2001).
12. Mangles S., Murphy C., Najmudin Z., Thomas A., Collier J., Dangor A., Divall E., Foster P., Gallacher J., Hooker C., Jaroszynski D., Langley A., Mori W., Norreys P., Tsung F., Viskup R., Walton B., Krushelnick K. *Nature*, **431**, 535 (2004).
13. Litos M., Adli E., An W., Clarke C., Clayton C., Corde S., Delahaye J., England R., Fisher A., Frederico J., Gessner S., Green S., Hogan M., Joshi C., Lu W., Marsh K.A., Mori W.B., Muggli P., Vafaei-Najafabadi N., Walz D., White G., Wu Z., Yakimenko V., Yocky G. *Nature*, **515**, 92 (2014).
14. Tsymbalov I.N., Ivanov K.A., Shulyapov S.A., Krestovskih D.A., Volkov R.V., Savel'ev A.B., Ksenofontov P.A., Brantov A.V., Bychenkov V.Yu. *Proc. Int. Conf. LO'2016* (St.-Petersburg, 2016) R5.
15. Basov N.G., Zakharenkov Yu.A., Rupasov A.A., Sklizkov G.V., Shikanov A.S. *Diagnostika plotnoi plazmy (Dense Plasma Diagnostics)* (Moscow: Nauka, 1989).
16. Kalal M., Krupka M., Dostal J., Dudzak R., Ullschmied J. *Proc. 1st ECPD* (Frascati (Rome), Italy, 2015) Vol. 1, p. 14.
17. Dromey B., Kar S., Zepf M., Foster P. *Rev. Sci. Instrum.*, **75**, 645 (2004).
18. Wood W.M., Siders C.W., Downer M.C. *Phys. Rev. Lett.*, **67**, 3523 (1991).
19. Kalal M., Nugent K. *Appl. Opt.*, **27**, 1956 (1988).
20. Born M., Wolf E. *Principles of Optics* (Oxford: Pergamon Press, 1964; Moscow: Nauka 1973).
21. Hipp M., Woisetschläger J., Reiterer P., Neger T. *Measurement*, **36**, 53 (2004).
22. Alexandrov A.F., Bogdankevich L.S., Rukhadze A.A. *Principles of Plasma Electrodynamics* (Berlin, Heidelberg, New York: Springer Verlag, 1984; Moscow: Vysshaya Shkola, 1988).
23. Balazs L., Gijbels R., Vertes A. *Anal. Chem.*, **63**, 315 (1991).
24. Moscicki T., Hoffman J., Szymanski Z. *Arch. Mechanics*, **63**, 99 (2011).
25. Cai H., Mima K., Sunahara A., Johzaki T., Nagatomo H., Zhu S., He X. *Phys. Plasmas*, **17**, 023106 (2010).
26. Kruer W., Estabrook K. *Phys. Fluids*, **28**, 430 (1985).
27. Sheng Z., Mima K., Zhang J., Meyer-ter-Vehn J. *Phys. Rev. E*, **69**, 016407 (2004).
28. Berge L., Soulez C-L., Köhler C., Skupin S. *Appl. Phys. B*, **103**, 563 (2011).
29. Landau L.D., Lifshits E.M. *Quantum Mechanics* (Oxford: Pergamon Press, 1977; Moscow: Fizmatlit, 2004).